# *Supplementary Material*: Thermal Boundary Conductance Across Epitaxial Metal/Sapphire Interfaces

Yee Rui Koh[1†], Jingjing Shi[2†], Baiwei Wang[3], Renjiu Hu[4], Habib Ahmad[5], Sit Kerdsongpanya[3], Erik Milosevic[3], W. Alan Doolittle[5], Daniel Gall[3], Zhiting Tian[4], Samuel Graham[2,6&], and Patrick E. Hopkins[1,7,8*]

[1]*Department of Mechanical and Aerospace Engineering, University of Virginia, Charlottesville, Virginia 22904, USA*
[2]*George W. Woodruff School of Mechanical Engineering, Georgia Institute of Technology, Atlanta, Georgia 30332, USA*
[3]*Department of Materials Science and Engineering, Rensselaer Polytechnic Institute, Troy, New York 12180, USA*
[4]*Sibley School of Mechanical and Aerospace Engineering, Cornell University, Ithaca, New York 14853, USA*
[5]*School of Electrical and Computer Engineering, Georgia Institute of Technology, Atlanta, GA, 30332, United States*
[6]*School of Materials Science and Engineering, Georgia Institute of Technology, Atlanta, Georgia 30332, USA*
[7]*Department of Materials Science and Engineering, University of Virginia, Charlottesville, Virginia 22904, USA*
[8]*Department of Physics, University of Virginia, Charlottesville, Virginia 22904, USA*

Corresponding authors: *phopkins@virginia.edu, and &sgraham@gatech.edu

†Author contributes equal contribution to the paper.

**Molecular-beam Epitaxy (MBE) Grown Al/sapphire Interface**

Aluminium was thermally evaporated in a MBE chamber on single side polished c-plane sapphire substrates at a substrate temperature of 200 °C and $10^{-10}$ torr. Before deposition, the 2" diameter zero miscut c-plane sapphire wafer was annealed in a Minibrute furnace using a multi-step annealing method. The c-plane sapphire wafer was first introduced into the furnace front zone at 1000 °C under nitrogen environment for 5 minutes. Subsequently, the wafer was moved into the center zone of the furnace and annealed at 1075 °C under nitrogen environment for 15 minutes and under Ultra Zero Grade (UZG) air environment for one hour. The furnace temperature was then ramped up to 1175 °C and the c-plane sapphire wafer was annealed at this temperature under UZG air for 5 hours. The wafer was then naturally cooled down under nitrogen overnight. This multi-step, high temperature annealing process reduced the surface energy of sapphire and resulted in a terrace-and-step structure on the sapphire surface. Annealing improved the Root Mean Square

(RMS) roughness of c-plane sapphire from 0.4 nm to 0.05 nm. The terraces are 550 nm wide with a step height of 0.3 nm. These terraces act as nucleation sites for subsequent growth of Al layers. The unpolished side of annealed wafer was subsequently metalized with Tantalum using Unifilm DC sputterer for uniform heating during growth. The annealed and metalized c-plane sapphire wafer was subsequently diced into 1 cm x 1 cm templates. These templates were piranha (solution of sulfuric acid and hydrogen peroxide in a ratio of 3 to 1) cleaned at a temperature of 150 °C for 10 minutes. The cleaned 1 cm x 1 cm c-plane sapphire substrate was then loaded into the load lock chamber of a Riber 32 MBE system and thermally cleaned under vacuum at 200 °C for 20 minutes. The substrate was then transferred into the main chamber of the MBE system and outgassed at 800 °C for 10 minutes. 80 nm of Al was grown on the c-plane sapphire substrate by thermal evaporation from a conventional Veeco effusion cell at a substrate temperature of 200 °C. X-ray Diffraction (XRD) showed Al (111) orientation of the deposited film on c-plane annealed sapphire substrate. The Reflection High Energy Electron Diffraction (RHEED) and Atomic Force Microscopy (AFM) images on the Al/sapphire are presented in the Figure S1 (a) and (b) respectively and show the high surface smoothness.

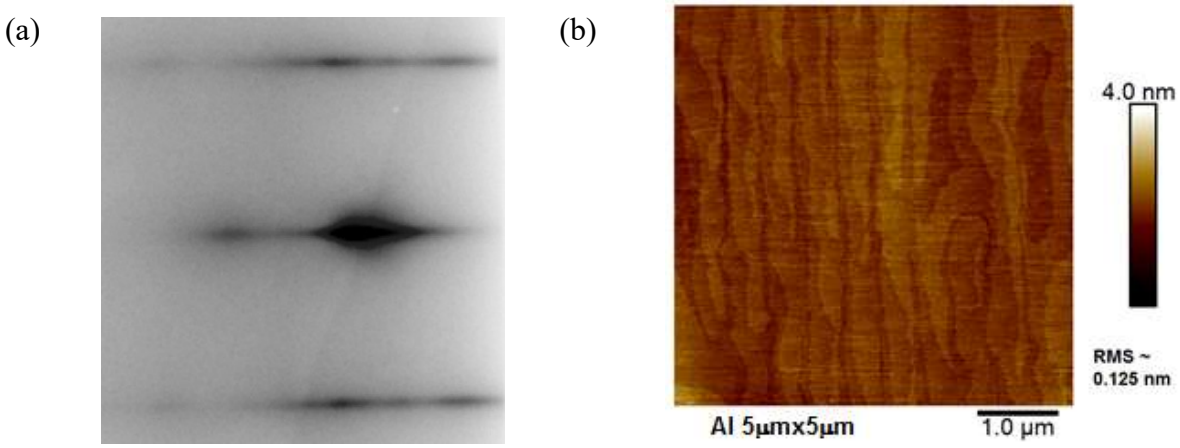


Figure S1 (a) Reflection High Energy Electron Diffraction (RHEED) image of the grown Al film. Streaky RHEED pattern is observed which shows high surface smoothness. (b) AFM images of the Al layer on the sapphire substrate. The RMS surface roughness of 0.125 nm for 5 µm x 5 µm image.

**Magnetron Sputtering Grown TiN/MgO, Co/sapphire and Ru/sapphire Interfaces**

Epitaxial Ru(0001)/$Al_2O_3$(0001), Co(0001)/$Al_2O_3$(0001), and TiN(001)/MgO(001) layers were deposited by magnetron sputtering in a load-locked ultra-high vacuum deposition system with a base pressure of $10^{-9}$ Torr described in detail elsewhere. [66] Single-side polished 10×10×0.5 $mm^3$ single-crystal $Al_2O_3$(0001) and MgO(001) substrates were cleaned in sequential ultrasonic baths of tri-chloroethylene, acetone, and isopropyl alcohol, for 20 min each, rinsed in de-ionized water, blown dry with nitrogen, mounted onto a Mo substrate holder using silver paint, and inserted into the deposition system. Prior to deposition, substrates were degassed for 1 hour, at 1000 °C for MgO and 300 °C for $Al_2O_3$, using a radiative pyrolytic graphite heater. Subsequently, the heater current was adjusted to reach the desired substrate temperature, which is 350 °C for Ru[43], 300 °C for Co[44], and 600 °C for TiN[45], as measured by a thermocouple underneath the substrate holder that was cross-calibrated with a pyrometer focused on the substrate surface. For the deposition of cubic TiN by reactive sputtering, 99.999% pure $N_2$ was further purified with a MicroTorr purifier and introduced into the chamber with a needle valve to reach a constant pressure of 5 mTorr, as measured with a capacitance manometer. A constant power of 100 W was applied to a 5.1-cm-diameter 99.99% Ti target, yielding a growth rate of 1.4 nm/min and a thickness of 55 nm, as determined by X-ray reflectivity. Hexagonal Ru (Co) layers were deposited in 3.0 mTorr 99.999% Ar using a power of 60 W (50 W) to a 99.95% Ru (Co) target, yielding a growth rate of 12.6 (30) nm/min and a thickness of 78 (118) nm. *In situ* annealing was used to further improve the crystalline quality after deposition. Ru films were annealed using a temperature ramp up to 1000 °C for a total of 3 hours, and Co films were annealed at 500 °C for one hour[46]. The substrates were continuously rotated at 60 rpm during the deposition of all layers to ensure composition and thickness uniformity.

X-ray diffraction was done with a Panalytical X'Pert PRO MPD system with a Cu Kα source and a hybrid mirror with a two-bounce two-crystal Ge(220) monochromator, yielding a parallel incident beam with a wavelength $\lambda_{K\alpha 1}$ = 1.5406 Å, a divergence of 0.0068°, and a width of 0.3 mm. Sample alignment included height adjustment as well as correction of the $\omega$ and $\chi$ tilt angles by maximizing the substrate peak intensity. Symmetric $\omega$-$2\theta$ scans were obtained using a 0.04 radian Soller slit in front of a PIXcel solid-state line detector operated in receiving mode with a 0.165 mm active length, corresponding to a $2\theta$ opening of less than 0.04°. $\omega$-rocking curves were obtained using constant $2\theta$ angles corresponding to 002 reflections for TiN and 0002 for Co and

Ru, with the same parallel beam geometry as used for $\omega$-$2\theta$ scans. $\omega$-$2\theta$ scans with a divergent beam Bragg-Brentano geometry were acquired over a large $2\theta$ range covering 10-85° in order to detect small inclusions of possible secondary phases or misoriented grains, as described in more detail in previous publications. [43,44,45,46,47] Typical asymmetric high-resolution reciprocal space maps (HR RSM) around 113 reflections of TiN, taken as an example in the results part, were obtained using a small angle (10-14°) between the sample surface and the diffracted beam to cause beam narrowing which increases the $2\theta$ resolution and therefore facilitates fast high-resolution reciprocal space mapping by taking advantage of parallel acquisition with all 255 channels of a line detector operated in scanning mode.

The Ru(0001), Co(0001), and TiN(001) layers are all epitaxial single-crystalline layers, as determined by a series of x-ray diffraction (XRD) measurements. [43,44,45,46,47] Figure S2 illustrates the XRD analysis for a 54.4 nm thick TiN/MgO(001) layer. The only detected reflections over the measured $2\theta$ range between 10° - 80° are the MgO 002 and TiN 002 at 42.91° and 42.50°, respectively, as shown in the pattern plotted in Figure S2(a) for $2\theta$ = 41.4° - 43.1°. The TiN peak position corresponds to an out-of-plane lattice constant $a_\perp$ = 4.251 Å which is within the range of previously reported values of 4.233-4.277 Å for epitaxial TiN/MgO(001) layers, [48,49,50,51,52,53,54] but is larger than the majority of reported values ranging from 4.240-4.249 Å. The relatively large $a_\perp$ is due to biaxial compressive misfit strain, as described below. The pattern exhibits Laue oscillations (layer thickness fringes) which indicate a relatively high crystalline quality and provide a value for the TiN layer thickness of 55 nm,[67] in good agreement with $d$ = 54.4 nm obtained from x-ray reflectivity measurements. The inset shows the $\omega$ rocking curve for the TiN 002 reflection. The narrow full-width at half-maximum (FWHM) of $\Gamma_\omega$ = 0.06° indicates a good crystalline quality. Corresponding $\Gamma_\omega$ values from other reported epitaxial rock-salt structure nitride layers range from 0.14 – 2.20°. [48,68,69,70,71,72,73,74]

Figure S2(b) shows a typical high-resolution XRD reciprocal space map acquired about asymmetric 113 reflections from the TiN(001)/MgO(001) layer.[45] The diffracted intensity distribution is plotted as color filled iso-intensity contour map in a logarithmic scale, as a function of the reciprocal lattice vector $k_\perp$ perpendicular and $k_\parallel$ parallel to the surface. The TiN out-of-plane $a_\perp$ and in-plane $a_\parallel$ lattice constants are determined from the peak positions $k_\perp$ = 7.053 nm$^{-1}$ and $k_\parallel$ = 3.358 nm$^{-1}$, yielding $a_\perp = 3/k_\perp$ = 4.254 ± 0.001 Å and $a_\parallel$ = sqrt(2)/$k_\parallel$ = 4.211 ± 0.001 Å. The

former value is in good agreement with 4.251 Å determined from the $\omega$-$2\theta$ scan, and the latter value matches, within the experimental uncertainty, the MgO lattice constant of 4.212 Å. This indicates that the TiN layer is fully strained, that is, its lattice is coherent with that of the substrate, which is also directly evident from the vertical alignment of the MgO and TiN 113 reflections in Figure S2(b). The layer is under a compressive strain $\varepsilon_{\|} = (a_{\|}/a_o - 1) = -0.64\%$, where the relaxed lattice constant $a_o$ is determined using $a_o = (a_\perp - \nu a_\perp + 2\nu a_{\|})/(1 + \nu) = 4.238$ Å and is the Poisson's ratio $\nu = 0.22$. [54,75] The elliptical shape of the TiN 113 reflection in reciprocal space can be described by peak broadening along the two primary directions $k_\perp$ and $k_{\|}$, with a FWHM of $\Delta k_\perp = 0.018$ nm$^{-1}$ and $\Delta k_{\|} = 0.006$ nm$^{-1}$. These values are in excellent agreement with $\Delta k_\perp = \Gamma_{2\theta}\cos\theta/\lambda = 0.017$ nm$^{-1}$ and $\Delta k_{\|} = 2\Gamma_\omega \sin\theta/\lambda = 0.005$ nm$^{-1}$, determined using the peak width $\Gamma_{2\theta}$ and $\Gamma_\omega$ from the symmetric $\omega$-$2\theta$ and $\omega$ rocking curve scans of the TiN 002 reflection shown in Figure S2(a). Similar XRD analyses were performed on other layers, confirming that Ru(0001) and Co(0001) layers are epitaxial single crystals. The details of the analyses can be found in the Ref. [43], [44], and [46].

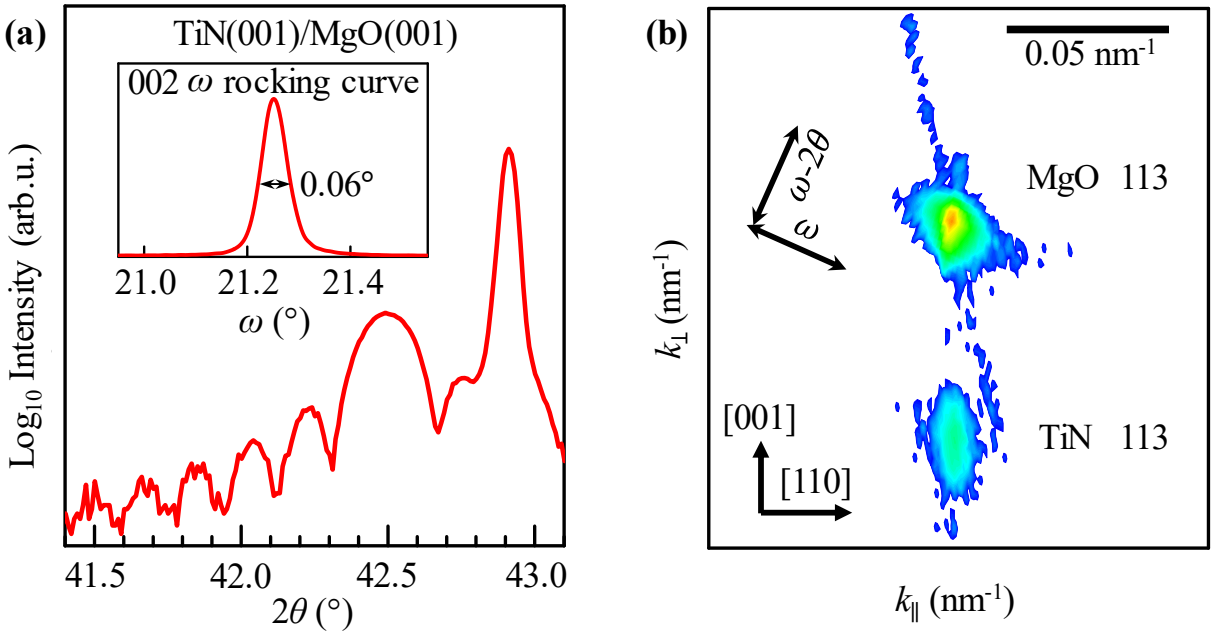


Figure S2 X-ray diffraction (a) $\omega$-$2\theta$ scan of 002 reflections and (b) HR-RSMs about asymmetric 113 reflections from an epitaxial TiN(001) layer grown on MgO(001).[45] Inset in (a) is the $\omega$ rocking curve of the TiN 002 reflection.

**Modal Non-equilibrium Landauer Approach with Transmission from Diffuse Mismatch Model (DMM)**

The Landauer approach is a commonly used method to predict thermal boundary conductance (TBC) across interfaces. The general form of the method is:

$$G = \frac{q}{\mathrm{A}\Delta T} = \frac{1}{\mathrm{A}\Delta T}\left( \sum_p \frac{A}{2} \iint D_1(\omega) f_{BE}\left(T_{\mathrm{in},1}\right) \hbar\omega v_1(\omega) \tau_{12}(\theta,\omega) \cos\theta \sin\theta \, d\theta d\omega \right.$$
$$\left. - \sum_p \frac{A}{2} \iint D_2(\omega) f_{BE}\left(T_{\mathrm{in},2}\right) \hbar\omega v_2(\omega) \tau_{21}(\theta,\omega) \cos\theta \sin\theta \, d\theta d\omega \right),$$

where the $\frac{1}{2}$ means half the phonons are traveling towards the interface, $q$ is the net heat flow rate, $A$ is the cross-sectional area of the interface, $\Delta T$ is the temperature drop across the interface, $D$ is the phonon density of states, $f_{BE}$ is the Bose-Einstein distribution function to describe the carrier statistics of phonons, $T_{\mathrm{in},1}$ and $T_{\mathrm{in},2}$ are the temperature of the incident phonon towards the interface from material 1 and 2, respectively, $\hbar$ is the reduced Planck constant, $\omega$ is the phonon angular frequency, $v$ is the phonon group velocity, $\tau_{12}$ is the transmission coefficient from material 1 to 2 across the interface, $\theta$ is the angle of incidence, and the sum is over all phonon polarizations. Here we applied the diffuse mismatch model (DMM) to calculate the transmission coefficient at the interface, because DMM usually works better when compared with experiments at most interfaces. The DMM transmission is independent of incident angle and also the principle of detailed balance, the expression of TBC can be simplified as:

$$G = \frac{\sum_p \frac{1}{4} \int D_1(\omega) \left( f_{BE}\left(T_{\mathrm{in},1}\right) - f_{BE}\left(T_{\mathrm{in},2}\right) \right) \hbar\omega v_1(\omega) \tau_{12}(\omega) d\omega}{\Delta T},$$

and the transmission function from DMM is:

$$\tau_{12}(\omega) = \frac{\sum_p M_2(\omega)}{\sum_p M_1(\omega) + \sum_p M_2(\omega)},$$

where $M$ is the phonon number of modes for a certain frequency, and for 3D isotropic material, it is proportional to the square of the wavenumber. Transmission of the Al, Co, and Ru are shown in the Figure

S3 (a) below. We also show the corresponding spectral accumulation TBC versus phonon frequency in Figure S3 (b).

It has been observed that the original Landauer formula usually underestimate the TBC at interfaces. One of the reasons which lead to the underestimation is the local non-equilibrium phonon transport effect at the interface, that the local temperature drop across the interface is smaller than the temperature difference between incident phonon temperatures from two materials, which means that $\Delta T < T_{\mathrm{in},1} - T_{\mathrm{in},2}$. This non-equilibrium effect can be included in the modal non-equilibrium Landauer approach and the method has been applied to all the systems we studied.

From the modal non-equilibrium Landauer formula, the TBC is:

$$G_{\mathrm{non-equilibrium}} = \frac{\sum_p \frac{1}{4} \int D_1(\omega) \left( f_{BE}(T_{\mathrm{in},1}) - f_{BE}(T_{\mathrm{in},2}) \right) \hbar \omega v_1(\omega) \tau_{12}(\omega) d\omega}{T_1 - T_2},$$

where $T_1$ and $T_2$ are the local equivalent equilibrium temperature right across the interface in material 1 and 2, respectively. $T_1$ and $T_2$ can be calculated from the modal transmission coefficient and other phonon properties of material 1 and 2. [26]

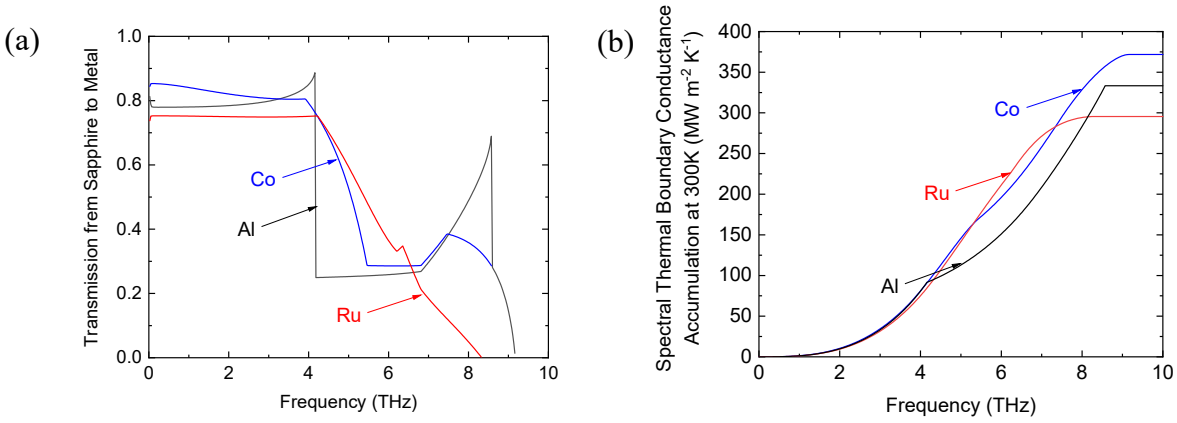


Figure S3 (a) The calculated transmission from sapphire to the Al, Ru and Co and (b) spectral accumulation TBC versus phonon frequency.

**Atomistic Green Function (AGF)**

Atomistic Green's function (AGF) is a widely used method to calculate the transmission and related thermal properties of a system. Some details are available in other papers[76-78]. Generally, the system (Figure S4) consists of three parts: two leads of semi-infinite length (L & R) and a central region with finite size (C). In this case, L is metals (Al or Ru), R is bulk sapphire. Figure S4 (a) and (b) are plots via VESTA[79]. Under harmonic assumption, the transmission of the system is

$$\Xi(\omega) = \mathbf{Tr}(\Gamma_L(\omega)G_C(\omega)\Gamma_R(\omega)G^{\dagger}(\omega))$$

where $\Gamma_{\alpha=L,R}$ is the level-width function of the leads and $G_C$ is the Green's function of the central region. Consequently, the thermal conductance should be presented as

$$\sigma(T) = \int_0^{\infty} \hbar\omega \frac{\partial f(\omega,T)}{\partial T} \Xi(\omega) \frac{\mathrm{d}\omega}{2\pi}$$

where $f(\omega,T)$ is the Bose-Einstein distribution.

In this paper, the second-order DFT force constants of the leads and the interface are obtained individually from the frozen-phonon method[80,81] using QUANTUM ESPRESSO[82] and Phonopy[83]. We use hexagonal unit cell of aluminium to calculate the thermal conductance along the Al[111]/sapphire[0001] direction, and we calculated the thermal conductance along the Ru[0001]/sapphire[0001]. We expand the lattice constant of Ru unit cell to match the unit cell of sapphire. To consider the interfacial interactions, the force constants of Al/sapphire and Ru/sapphire interfaces were directly gained from DFT calculation. We use one unit cell of Al/Ru and 6 atom layers from sapphire to build the interface, and we add vacuum on both sides to make sure it is a single interface. The unit cell of the metal/sapphire interface structures have shown in Figure S4. We used projector augmented-wave method[84] of Perdew, Burke and Ernzerhof[85] For the Ruthenium lead, the cut-off energy is 70 Ryd, and the *k* points mesh is $3 \times 3 \times 3$ for the $3 \times 3 \times 3$ supercell. While in the Aluminum lead, the cut-off energy is 50 Ryd, and the *k* points mesh is $4 \times 4 \times 3$ for the $3 \times 3 \times 3$ supercell. And for the sapphire lead, the cut-off energy is 80 Ryd, and the *k* points mesh is $4 \times 4 \times 2$ for the $3 \times 3 \times 2$ supercell. The cut-off energy of both interfaces is 100 Ryd and the *k* points mesh is $2 \times 2 \times 1$ for the $2 \times 2 \times 1$ supercell. To reflect the

in transverse direction, the transverse k points mesh is $20 \times 20$ in the Brillouin zone to ensure the convergence. The lattice constant of the Al and Ru is 4.9485Å and 4.8076Å respectively.

At the same time, to reveal the fact that temperature drops right across the interface rather than between source and sink, the modified thermal conductance is desired[86].

$$\sigma'(T) = \sigma(T) \times \frac{1}{1 - 0.5 \times [\frac{\sigma(T)}{\sigma_1(T)} + \frac{\sigma(T)}{\sigma_2(T)}]}$$

where $\sigma_1$ and $\sigma_2$ are the thermal conductance of pure material of bulk leads, and $\sigma$ is the thermal conductance of the interface.

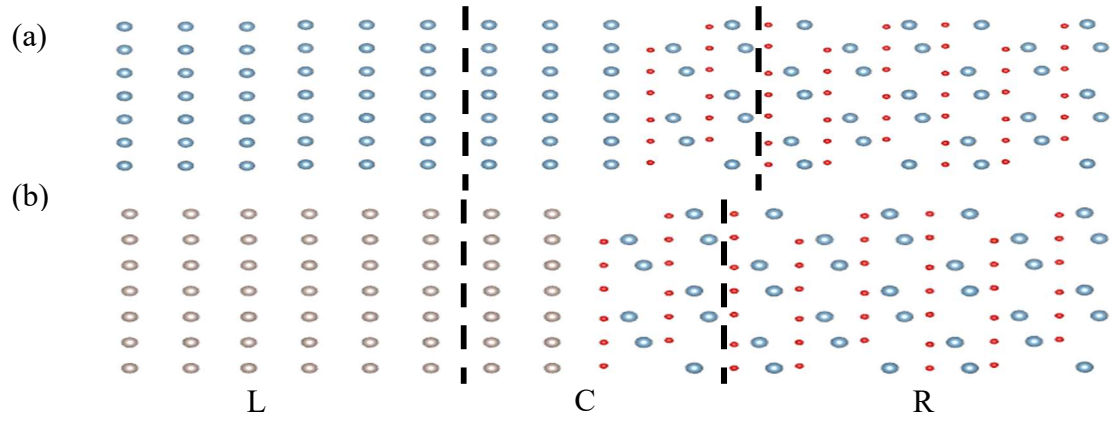


Figure S4 Schematic of the (a) Al/sapphire[18] and (b) Ru/Sapphire system. L, C and R refer to left lead, central region and right lead, correspondingly. The Al/sapphire system is based on the Ref. [[18]].

Transmission of the Al, and Ru via AGF method are shown in the Figure S5 (a) below. We also show the corresponding spectral accumulation TBC versus phonon frequency in Figure S5 (b).

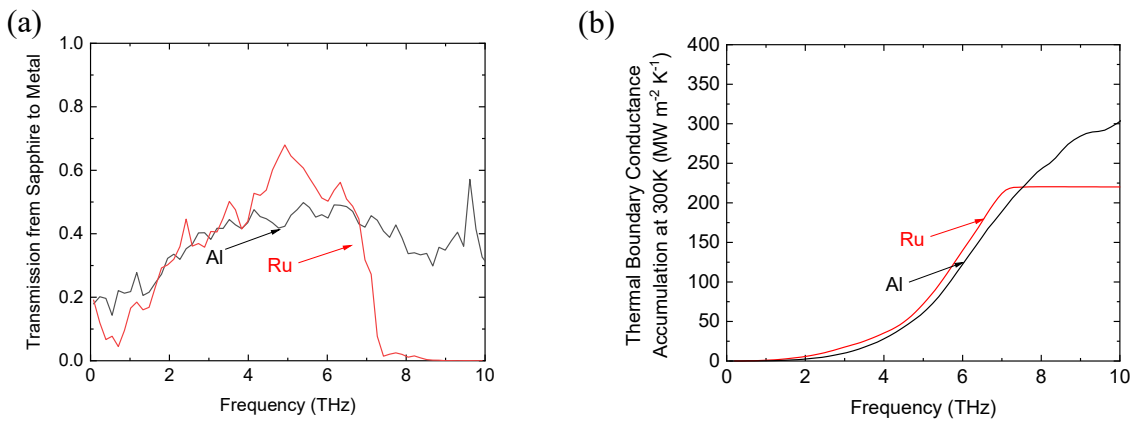


Figure S5 (a) The calculated transmission from sapphire to the Al, and Ru and (b) spectral accumulation TBC versus phonon frequency.

## Thermal Boundary Conductance (TBC) Measurements via Time-domain Thermoreflectance (TDTR)

We used TDTR to measure the TBC across the various Al/sapphire, Co/sapphire, Ru/sapphire and TiN/MgO interfaces as a function of temperature from ~80–500 K. The details of TDTR are discussed in Refs. [6], [7] and [8]. In TDTR, a Ti:Sapphire femtosecond laser creates sub-picosecond laser pulses at a central wavelength of ~800 nm (bandwidth ~10.5 nm) and a repetition rate of 12.5 ns. The laser pulses are split into a pump beam and a probe beam. We convert the central wavelength of the pump pulses to an ~400 nm central wavelength. The pump beam has a higher power than the probe to heat the sample surface and is modulated at a frequency of 8.8 MHz. At the sample surface, the radius of the focused pump spot is ~8 μm, while that of the probe is ~5 μm. The reflected probe beam signal from the sample surface was collected by a Si-photodetector and an RF lock-in amplifier, and we monitor both in-phase and out-of-phase voltages from the lock-in output. We then analyse the ratio of the in-phase to out-of-phase voltage generated from this reflected probe beam as a function of pump-probe delay time, and determine the TBC across the metal/sapphire interfaces by fitting the solution to a cylindrically symmetric, multilayer thermal diffusion model to our TDTR data. For these fits, we assume the thermophysical properties of the Al, Co, Ru and sapphire listed in Table SI. Details of TDTR analyses are found in Refs. [7] and [8]. The increase of the sample surface temperature during the measurements was limited to much less than 10 °C.

Table SI List of thermal properties of the Co, Al, Ru, and sapphire.

| | Sapphire | Co | Al | Ru |
|---|---|---|---|---|
| Thermal conductivity ($W\ m^{-1}\ K^{-1}$) | 28-35[87] | 111[88] | 190[89] | 109[90] |
| Volumetric heat capacity ($J\ cm^{-3}\ K^{-1}$) | 3.07[91] | 4.08[91,92] | 2.42[89] | 2.91[93] |

**Time-domain Thermoreflectance (TDTR) Sensitivity Analysis**

Using the sensitivity analysis, we can determine the most appropriate uncertainties for the measured thermal boundary conductance (TBC) of the Co/sapphire, Al/sapphire, Ru/sapphire, and TiN/MgO samples. Figure S6 (a)-(h) show the contour of the mean square deviation of the thermal model of the TDTR ratio ($-V_{in}/V_{out}$) as the function of TBC and substrate thermal conductivity, at ~80K and ~500K respectively. The innermost contour line indicates the combinations of the TBC and substrate thermal conductivity lie with 95% confidence interval. This confidence interval confirms the uncertainty bound or error bars of the measured TBC and substrate thermal conductivity. A confined range of the TBC of Co/sapphire, Al/sapphire, and Ru/sapphire can be obtained in the analysis. While, the uncertainty bound of the TiN/MgO is relatively big, especially in the TBC measurements above ~300K. In other word, the TBC measurements are insensitivity in TiN/MgO at high temperature regime. Therefore, we do not present the exact value of the TiN/MgO above 400K in Figure 2 of the manuscript. Within the confidence interval, we could not differentiate the thermal resistances contributed by the thin film and interface.

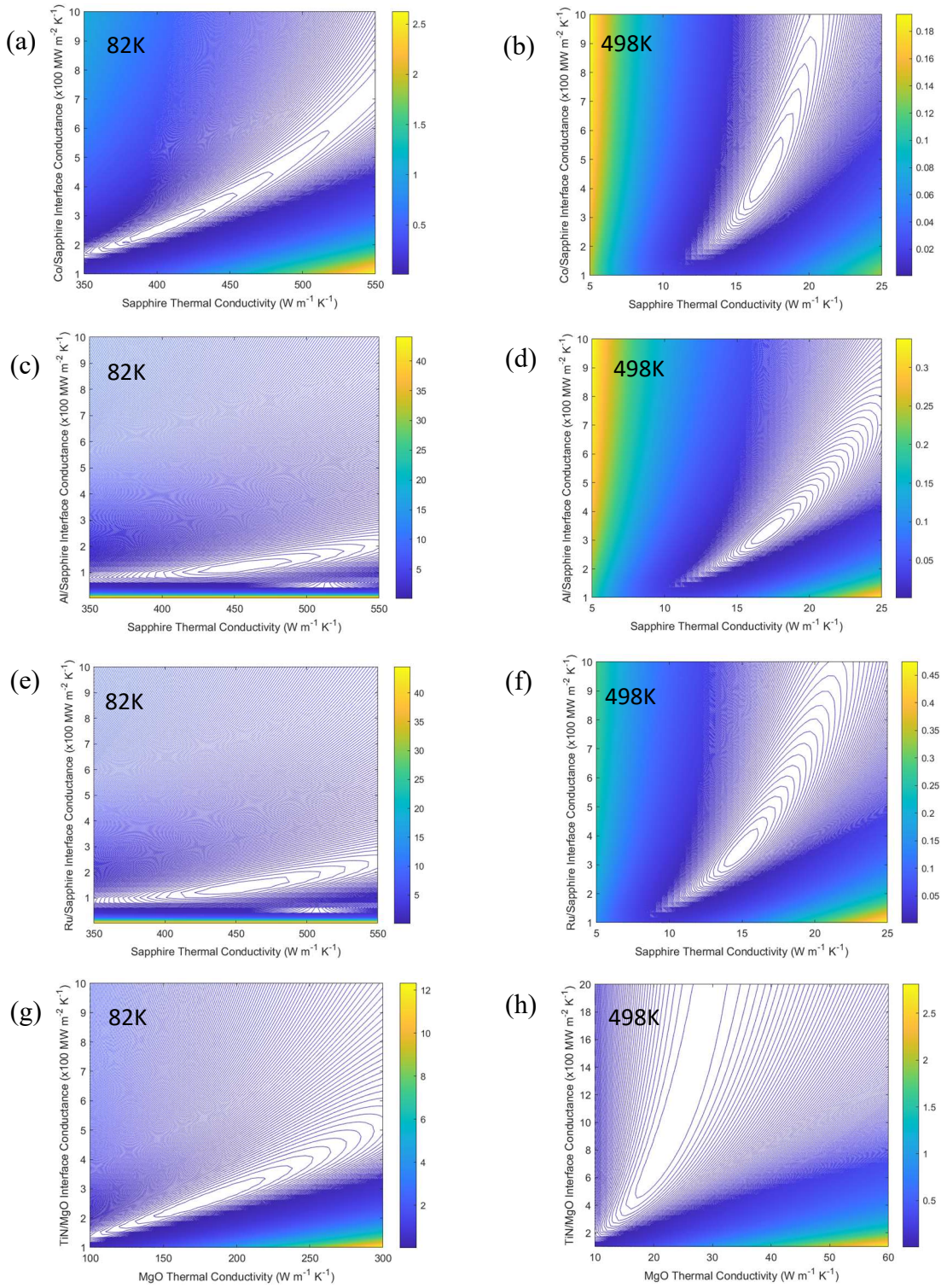


Figure S6 Sensitivity contour plots for the Co/sapphire, Al/sapphire, Ru/sapphire, and TiN/MgO, as a function of TBC and substrate thermal conductivity. Figures (a), (c), (e), and (g) are the analysis at ~80K, while figures (b), (d), (f), and (h) are the analysis at ~500K.

Figure S7 (a)-(d) show the results from contour plot analyses that demonstrate the mean square deviation of the thermal model to the TDTR data for various combinations of metal/substrate TBC and substrate thermal conductivity as input parameters in the model at room temperature.

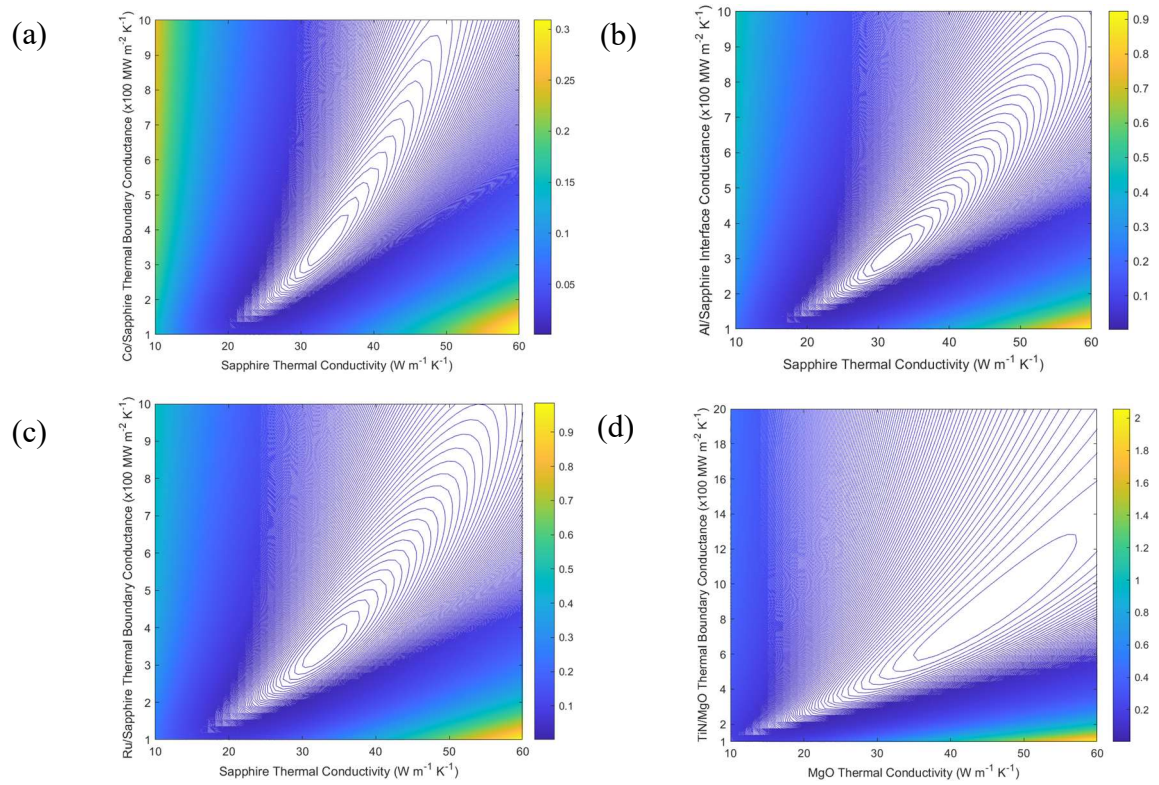


Figure S7 Sensitivity contour plots for (a) Co/sapphire, (b) Al/sapphire, (c) Ru/sapphire, and (d) TiN/MgO for TBC as a function of substrate thermal conductivity at room temperaturee. The lowest value of the contour lines indicates the combinations of thermal parameters that lie within a 95% confidence interval for the best thermal model fittings.

**Temperature Dependence Substrate Thermal Conductivity**

There are two main substrates, i.e. sapphire and MgO, are used in the project. We show the temperature dependence of the measured c-plane sapphire and MgO substrate thermal conductivity in Figure S8. We employed 8.8MHz pump modulation frequency in our TDTR measurements, with ~5.5μm probe radii and ~8 μm pump radii. The measured thermal conductivity is sensitivity to the cross-plane direction, which is vertical to the $Al_2O_3$(0001) and MgO(001) respectively. The

measured c-plane sapphire and MgO substrate thermal conductivity are well matched to the literature values in Ref. [18], [94] and [95].

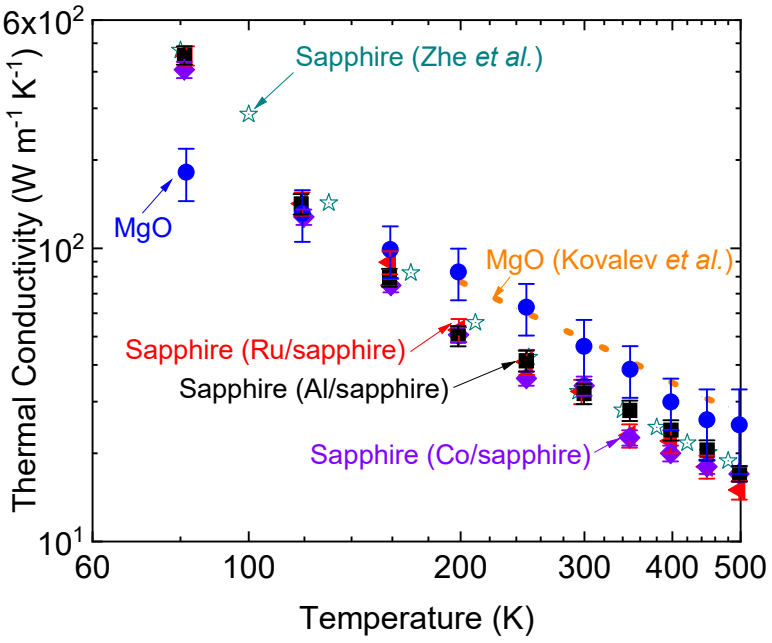


Figure S8 The temperature dependence of measured c-plane sapphire and MgO thermal conductivity.

**Annealing Effects on the Al/sapphire Sample via Molecular Beam Epitaxy (MBE)**

Figure S9 (a) shows 5μm x 5 μm Atomic Force Microscopy (AFM) image of the c-plane sapphire wafer before annealing. Figure S9 (b) shows 5μm x 5 μm AFM image of the c-plane sapphire wafer after annealing. The AFM images below show that annealing process improved the Root Mean Square (RMS) roughness of c-plane sapphire from 0.4 nm to 0.05 nm.

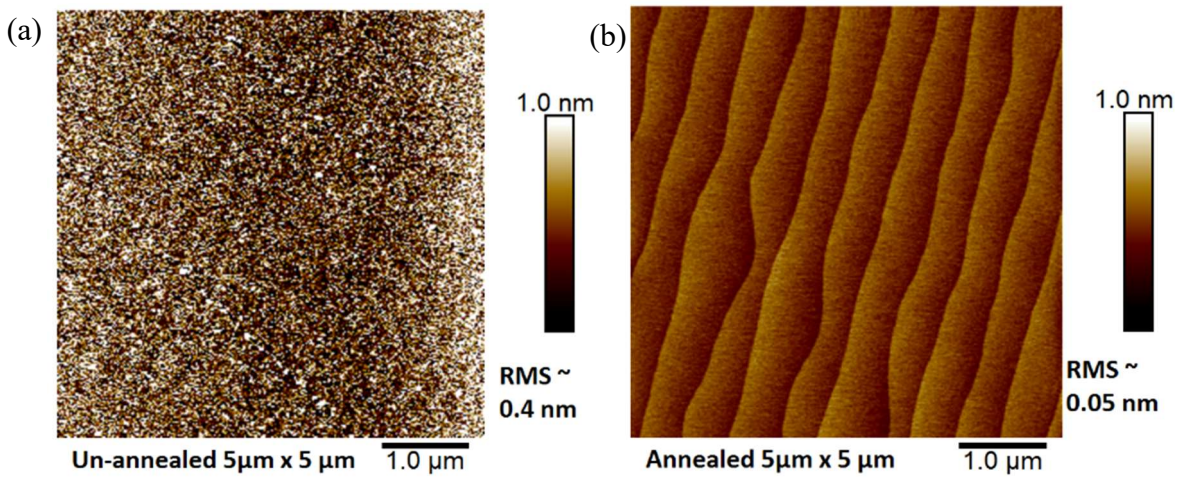


Figure S9 5µm x 5 µm AFM image of the sapphire wafer (a). Before annealing (b). After annealing

**XRD Analysis of the Co/sapphire, Ru/sapphire, and Al/sapphire**

The samples used in the project are grown by two different methods, i.e. magnetron sputtering and MBE. The Co/sapphire, and Ru/sapphire are grown with magnetron sputtering, while Al/sapphire is grown in MBE. We have included XRD analysis of these samples (reported in Ref. [43], [44], [46] and [18]) in Figure S10 below.

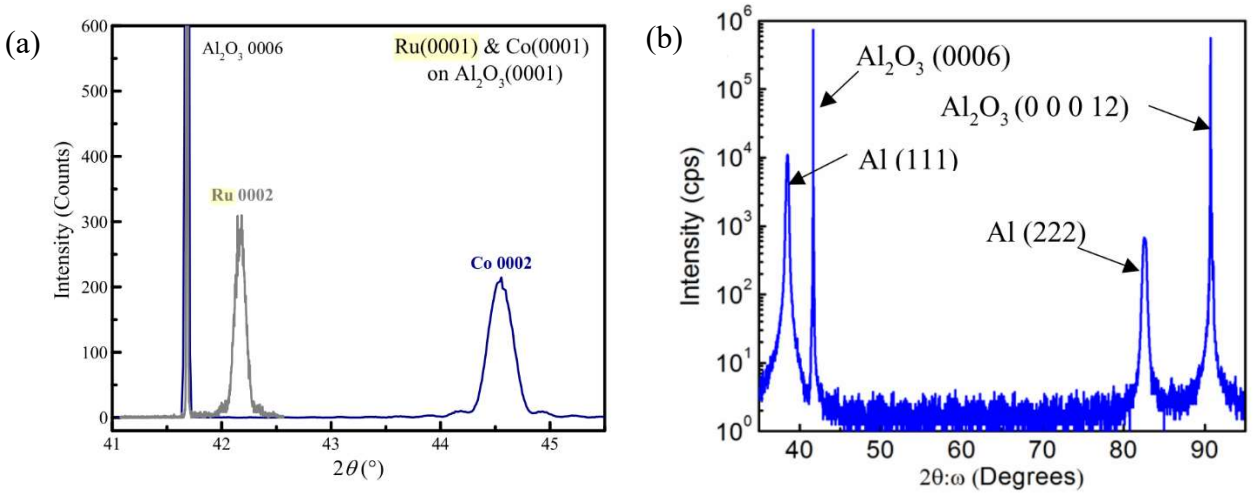


Figure S10 Overlaid representative θ-2θ diffractograms for epitaxial a) Ru(0001)/Al2O3(0001) and epitaxial Co(0001)/Al2O3(0001) [46], and b) Al(111)/Al2O3(0001)[18].

## References


6. Jiang, P., Qian, X. & Yang, R. Tutorial: Time-domain thermoreflectance (TDTR) for thermal property characterization of bulk and thin film materials. *Journal of Applied Physics* **124**, 161103 (2018).

7. Cahill, D. G. Analysis of heat flow in layered structures for time-domain thermoreflectance. *Rev. Sci. Instrum*. **75**, 5119–5122 (2004).

8. Schmidt, A. J., Chen, X. & Chen, G. Pulse accumulation, radial heat conduction, and anisotropic thermal conductivity in pump-probe transient thermoreflectance. *Rev. Sci. Instrum*. **79**, 114902 (2008).

18. Cheng, Z., Koh, Y. R., Ahmad, H., Hu, R., Shi, J., Liao, M. E., Wang, Y., Bai, T., Li, R., Lee, E., Clinton, E. A., Matthews, C. M., Engel, Z., Yates, Luo, T., Goorsky, M. S., Doolittle, W., Tian, Z., Hopkins, P. E., et al. Thermal Conductance Across Harmonic-matched Epitaxial Al-sapphire Heterointerfaces. *Commun. Phys*. **3**, 115 (2019) doi:10.1038/s42005-020-0383-6.

26. Shi, J., Yang, X., Fisher, T. S. & Ruan, X. Dramatic increase in the thermal boundary conductance and radiation limit from a Nonequilibrium Landauer Approach. *arXiv Condens. Matter* doi:arXiv:1812.07910v2 (2018).

43. Milosevic, E., Kerdsongpanya, S., Zangiabadi, A., Barmak, K., Coffey, K. R. & Gall, D. Resistivity size effect in epitaxial Ru(0001) layers. *J. Appl. Phys*. **124**, 165105 (2018).

44. Milosevic, E., Kerdsongpanya, S., McGahay, M. E., Zangiabadi, A., Barmak, K. & Gall, D. Resistivity scaling and electron surface scattering in epitaxial Co(0001) layers. *J. Appl. Phys.* **125**, 245105 (2019).

45. Wang, B. & Gall, D. Fully strained epitaxial Ti1−xMgxN(001) layers. *Thin Solid Films* **688**, 137165 (2019).

46. Milosevic, E., Kerdsongpanya, S. & Gall, D. The Resistivity Size Effect in Epitaxial Ru(0001) and Co(0001) Layers. *2018 IEEE Nanotechnol. Symp. (ANTS)*, Albany, NY, USA, 1–5 (2018) doi:10.1109/NANOTECH.2018.8653560.

47. Wang, B. & Gall, D. A new semiconductor: Ti0.5Mg0.5N(001). *2018 IEEE Nanotechnol. Symp. (ANTS)*, Albany, NY, USA, 1-5 (2018) doi:10.1109/NANOTECH.2018.8653564.

48. Gall, D., Petrov, I., Desjardins, P. & Greene, J. E. Microstructural evolution and Poisson ratio of epitaxial ScN grown on TiN(001)/MgO(001) by ultrahigh vacuum reactive magnetron sputter deposition. *J. Appl. Phys.* **86**, 5524–5529 (1999).

49. Gall, D., Petrov, I. & Greene, J. E. Epitaxial Sc1−xTixN(001): Optical and electronic transport properties. *J. Appl. Phys*. **89**, 401–409 (2001).

50. Chawla, J. S., Zhang, X. Y. & Gall, D. Effective electron mean free path in TiN(001). *J. Appl. Phys*. **113**, 063704 (2013).

51. Chawla, J. S., Zhang, X. Y. & Gall, D. Epitaxial TiN(001) wetting layer for growth of thin

single-crystal Cu(001). *J. Appl. Phys*. **110**, 043714 (2011).

52. Wall, M. A., Cahill, D. G., Petrov, I., Gall, D. & Greene, J. E. Nucleation kinetics during homoepitaxial growth of TiN(001) by reactive magnetron sputtering. *Phys. Rev. B* **70**, 35413 (2004).

53. Shin, C. S., Gall, D., Hellgren, N., Patscheider, J., Petrov, I. & Greene, J. E. Vacancy hardening in single-crystal TiNx(001) layers. *J. Appl. Phys.* **93**, 6025–6028 (2003).

54. Shin, C. S., Rudenja, S., Gall, D., Hellgren, N., Lee, T. Y., Petrov, I. & Greene, J. E. Growth, surface morphology, and electrical resistivity of fully strained substoichiometric epitaxial TiNx ($0.67 \leqslant x < 1.0$) layers on MgO(001). *J. Appl. Phys*. **95 (1)**, 356–362 (2004).

66. Wang, B., Kerdsongpanya, S., McGahay, M. E., Milosevic, E., Patsalas, P. & Gall, D. Growth and properties of epitaxial Ti 1− x Mg x N(001) layers. *J. Vac. Sci. Technol. A* **36**, 061501 (2018).

67. Ingason, A. S., Magnus, F., Olafsson, S. & Gudmundsson, J. T. Morphology of TiN thin films grown on MgO(001) by reactive dc magnetron sputtering. *J. Vac. Sci. Technol. A* **28**, 912–915 (2010).

68. Zhang, K., Balasubramanian, K., Ozsdolay, B. D., Mulligan, C. P., Khare, S. V., Zheng, W. T. & Gall, D. Growth and mechanical properties of epitaxial NbN(001) films on MgO(001). *Surf. Coatings Technol.* **288**, 105–114 (2016).

69. Ozsdolay, B. D., Mulligan, C. P., Guerette, M., Huang, L. & Gall, D. Epitaxial growth and properties of cubic WN on MgO(001), MgO(111), and Al2O3(0001). *Thin Solid Films* **590**, 276–283 (2015).

70. Deng, R., Zheng, P. Y. & Gall, D. Optical and electron transport properties of rock-salt Sc1-xAlxN. *J. Appl. Phys*. **118**, 015706 (2015).

71. Deng, R., Ozsdolay, B. D., Zheng, P. Y., Khare, S. V. & Gall, D. Optical and transport measurement and first-principles determination of the ScN band gap. *Phys. Rev. B - Condens. Matter Mater. Phys*. **91**, 045104 (2015).

72. Ozsdolay, B. D., Shen, X., Balasubramanian, K., Scannell, G., Huang, L., Yamaguchi, M. & Gall, D. Elastic constants of epitaxial cubic MoNx(001) layers. *Surf. Coatings Technol.* **325**, 572–578 (2017).

73. Gall, D., Shin, C. S., Haasch, R. T., Petrov, I. & Greene, J. E. Band gap in epitaxial NaCl-structure CrN(001) layers. *J. Appl. Phys*. **91**, 5882–5886 (2002).

74. Shin, C. S., Gall, D., Kim, Y. W., Desjardins, P., Petrov, I., Greene, J. E., Odén, M. & Hultman, L. Epitaxial NaCl structure δ-TaNx(001): Electronic transport properties, elastic modulus, and hardness versus N/Ta ratio. *J. Appl. Phys.* **90**, 2879–2885 (2001).

75. Zhang, K., Balasubramanian, K., Ozsdolay, B. D., Mulligan, C. P., Khare, S. V., Zheng, W. T. & Gall, D. Epitaxial NbCxN1-x(001) layers: Growth, mechanical properties, and electrical resistivity. *Surf. Coatings Technol*. **277**, 136–143 (2015).

76. Mingo, N. & Yang, L. Phonon transport in nanowires coated with an amorphous material: An atomistic Green's function approach. *Phys. Rev. B - Condens. Matter Mater. Phys*. **68**, 245406 (2003).

77. Zhang, W., Fisher, T. S. & Mingo, N. Simulation of Interfacial Phonon Transport in Si–Ge Heterostructures Using an Atomistic Green's Function Method. *J. Heat Transfer* **129(4)**, 483-491 (2007).

78. Zhang, W., Mingo, N. & Fisher, T. S. Simulation of phonon transport across a non-polar nanowire junction using an atomistic Green's function method. *Phys. Rev. B - Condens. Matter Mater. Phys*. **76**, 195429 (2007).

79. Momma, K. & Izumi, F. VESTA 3 for three-dimensional visualization of crystal, volumetric and morphology data. *J. Appl. Crystallogr*. **44**, 1272–1276 (2011).

80. Esfarjani, K., Chen, G. & Stokes, H. T. Heat transport in silicon from first-principles calculations. *Phys. Rev. B - Condens. Matter Mater. Phys*. **84**, 085204 (2011).

81. Tian, Z., Garg, J., Esfarjani, K., Shiga, T., Shiomi, J. & Chen, G. Phonon conduction in PbSe, PbTe, and PbTe 1-xSe x from first-principles calculations. *Phys. Rev. B - Condens. Matter Mater. Phys*. **85**, 184303 (2012).

82. Giannozzi, P., Baroni, S., Bonini, N., Calandra, M., Car, R., Cavazzoni, C., Ceresoli, D., Chiarotti, G. L., Cococcioni, M., Dabo, I., Dal Corso, A., De Gironcoli, S., Fabris, S., Fratesi, G., Gebauer, R., Gerstmann, U., Gougoussis, C., Kokalj, A., Lazzeri, M., et al. QUANTUM ESPRESSO: A modular and open-source software project for quantum simulations of materials. *J. Phys. Condens. Matter* **21(39)**, 395502 (2009).

83. Togo, A. & Tanaka, I. First principles phonon calculations in materials science. *Scr. Mater*. **108**, 1-5 (2015) doi:10.1016/j.scriptamat.2015.07.021.

84. Blöchl P. E. Projector augmented-wave method. *Phys. Rev. B. Condens. Matter* **50**, 17953–17979 (1994).

85. Perdew, J. P., Burke, K. & Ernzerhof, M. Generalized gradient approximation made simple. *Phys. Rev. Lett.* **77**, 3865–3868 (1996).

86. Tian, Z., Esfarjani, K. & Chen, G. Enhancing phonon transmission across a Si/Ge interface by atomic roughness: First-principles study with the Green's function method. *Phys. Rev. B - Condens. Matter Mater. Phys*. **86**, 235304 (2012).

87. *Thermophysical Properties of High Temperature Solid Materials*. Purdue Research Foundation, NY, USA, (1967).

88. Montague, S. A., Draper, C. W. & Rosenblatt, G. M. Thermal diffusivities of hafnium and cobalt from 300 to 1000 K. *J. Phys. Chem. Solids* **40**, 987–992 (1979).

89. Valencia, J. J. & Corporation, C. T. Thermophysical Properties. Metal Process Simulation, ASM International 22B (2008). doi.org/10.31399/asm.hb.v22b.a0005523

90. Powell, R. W., Tye, R. P. & Woodman, M. J. The thermal conductivity and electrical resistivity of polycrystalline metals of the platinum group and of single crystals of

ruthenium. *J. Less-Common Met*. 12, 1–10 (1967).

91. Malcom W. Chase, J. NIST-JANAF Thermochemical Tables Fourth Edition. American Chemical Society and the American Institute of Physics for the National Institute of Standard and Technology, Woodbury, NY, USA (1998).

92. Sirota, N. N., Vinokurov, V. A. & Novikov, V. V. Heat capacity and thermodynamic functions of iron, cobalt, and nickel borides in the range of 5-300 K. *Zhurnal Fiz. Khimii* **72**, 785–789 (1998).

93. Furukawa, G. T., Reilly, M. L. & Gallagher, J. S. Critical Analysis of Heat Capacity Data and Evaluation of Thermodynamic Properties of Ruthenium, Rhodium, Palladium, Iridium, and Platinum from 0 to 300K. A Survey of the Literature Data on Osmium. *J. Phys. Chem. Ref. Data* **3**, 163–209 (1974).

94. Cahill, D. G., Lee, S. & Selinder, T. I. Thermal Conductivity of κ-Al2O3 and α-Al2O3 Wear-Resistant Coatings. *J. Appl. Phys*. **83**, 5783-5786 (1998).

95. Kovalev, N. N., Petrov, A. V. & Sorkin, O. V. Thermal Conductivity of Single Crystals of Barium, Strontium, Calcium, and Magnesium Oxides. *Sov. Phys. Solid State* **13**, 232–233 (1971).